Received: 6 April 2023 | Revised: 21 July 2023 | Accepted: 25 September 2023

DOI: 10.4218/etrij.2023-0142

ORIGINAL ARTICLE

ETRI Journal WILEY

Symbol interferometry and companding transform for PAPR reduction of OTFS signal

Aare Gopal[1] | **Desireddy Krishna Reddy**[2] | **Srinivasarao Chintagunta**[3]

[1]Department of Electronics and Communication Engineering, Osmania University, Hyderabad, Telangana, India

[2]Department of Electronics and Communication Engineering, CBIT, Hyderabad, Telangana, India

[3]Department of Electronics and Communication Engineering, National Institute of Technology Calicut, Kozhikode, Kerala, India

Correspondence
Aare Gopal, Department of Electronics and Communication Engineering, Osmania University, Hyderabad, Telangana, India.
Email: aaregopal@gmail.com

Abstract

This paper presents methods for reducing the peak-to-average power ratio (PAPR) of the orthogonal time frequency space (OTFS) signal. These methods mainly consist of two operations: symbol interferometry (SI) and either μ-law or A-law companding. SI spreads the data of one OTFS symbol onto all symbols and is implemented using a simple inverse fast Fourier transform operation on each OTFS symbol. During the second operation, the PAPR of the OTFS signal is significantly reduced. For our performance analysis, the complementary cumulative distribution function, probability density function, and bit error rate are illustrated through simulations performed in MATLAB. The performance is also analyzed using a solid-state power amplifier at the transmitter and compared with OTFS, μ-law-based OTFS, and SI OTFS systems. The results indicate that the proposed OTFS system achieves a low PAPR.

KEYWORDS

A-law companding, OTFS, PAPR, symbol interferometry, μ-law companding

1 | INTRODUCTION

Future-generation wireless networks are expected to support reliable communication in high-mobility scenarios (e.g., high-speed railway, drone, and vehicle-to-vehicle communications). The existing fourth- and fifth-generation communication technologies are based on orthogonal frequency-division multiplexing (OFDM) and offer considerable spectral efficiency for time-invariant channels. However, OFDM is not robust to time-varying channels, particularly in high-Doppler spreads. The new two-dimensional (2D) orthogonal time–frequency space (OTFS) modulation technology enables proper operations through time-varying channels [1, 2]. As such, the data points are multiplexed in the delay and Doppler domains rather than in the general time and frequency domains. The main process behind an OTFS system considers a time-varying wireless channel as a delay-Doppler (DD) type. In a DD channel, the time-varying wireless channel is treated as a time-invariant channel, which leads to improved performance over OFDM modulations.

Similar to OFDM [3–6], OTFS modulation exhibits a high peak-to-average power ratio (PAPR), whose mitigation has already been addressed [7–12]. The authors in [2] presented an analytical upper bound for the PAPR, considering that the size of one OTFS frame is $N_\tau \times N_v$, N_τ and N_v are the numbers of grids along the delay and Doppler dimensions, respectively. According to this upper bound [2], the PAPR of the OTFS modulation does not increase with the number of subcarriers (delay grids), as is the case with OFDM. However, the PAPR increases with the number of symbols (Doppler grids). This characteristic was verified using a complementary cumulative distribution function (CCDF) metric for the PAPR

variety [2]. Although the PAPR of an OTFS modulation is smaller than that of an OFDM modulation under $N_v < N_\tau$, it is desirable to reduce the PAPR of an OTFS modulation. However, few investigations of this issue have been reported in the literature [7–12]. Such investigations should be based on spreading codes with discrete Fourier transforms [7], iterative clipping and filtering [8], deep learning autoencoders [9], unique OTFS frame structures [10], Internet of Things (IoT) peak windowing techniques for railways [11], and nonlinear companding transforms [12–14]. The μ-law companding discussed in [12] performs better than clipping and reduces PAPR; however, it increases the average power, which is undesirable. The exponential companding transform in [13] exhibits poor bit error rate (BER) performance. In [14], the normalized μ-law and normalized A-law methods were examined, and the results showed that the normalized μ-law performed better than the normalized A-law, including the method covered in [12].

This study proposes a new method based on symbol interferometry (SI) coding [15] and μ-law and A-law companding to reduce the PAPR of the OTFS signal. This concept is based on the fast Fourier transform (FFT) carrier interferometry approach used in OFDM tasks [4]. The concept of carrier interferometry involves the dissemination of information from one subcarrier to all subcarriers. Because the PAPR of the OTFS varies with the number of symbols rather than the number of subcarriers [2], we implemented dissemination with respect to its symbols between the inverse symplectic FFT (ISFFT) and the Heisenberg transform. SI codes spread the data/energy of each symbol onto all symbols, thereby reducing the peak power. The SI operation can be performed using a simple inverse FFT (IFFT). The SI codes of the IFFT operation ensure orthogonality; thus, the despreading codes that use FFT perform undo operations with minimum or no reductions in BER performance. The PAPR of SI OTFS is further reduced by either the normalized μ-law [14] or normalized A-law companding [5, 14], which is applied to the time-domain signal after the Heisenberg transform. To validate the proposed method and compare it to existing methods, the CCDFs of PAPR, instantaneous-to-average power ratio (IAPR), probability density function (PDF), and BER are computed with simulations using the MATLAB tool.

The remainder of this paper is organized as follows: Section 2 describes the mathematical model of the proposed SI OTFS μ-law and A-law system. In Section 3, the simulation results and their discussions are presented. Finally, Section 4 presents our conclusions.

2 | MATHEMATICAL DESCRIPTION

OTFS modulation operates in the DD domain. Thus, constellation (i.e., information) points of M-ary quadrature amplitude modulations (QAMs) are considered in the DD domain. These DD information points are translated to the time–frequency domain using an ISFFT and then related to time domain using the Heisenberg transform. A cyclic prefix (CP) is added to avoid interference between OTFS frames, which are amplified using a high-power amplifier (HPA) prior to transmission. Consequently, after removing the CP at the receiver, the received signal in the time domain is transformed to the frequency–time domain using the Wigner transform and then to the DD domain using the symplectic FFT (SFFT). In the proposed system illustrated in Figure 1, we incorporated two blocks at the transmitter: SI/spreading (marked in blue) and either the μ-law or A-law (marked in red). Appropriate undo operation blocks are incorporated into the receiver, and the SI operation is performed using a simple IFFT on each symbol.

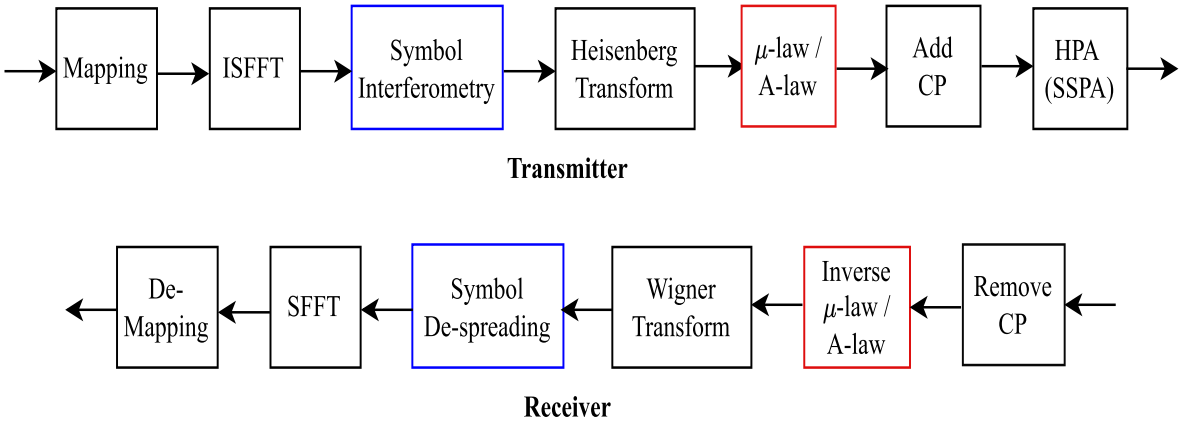

FIGURE 1 Block diagram of the proposed μ-law and A-law companded SI OTFS system.

To mathematically describe the proposed system shown in Figure 1, B is the total allocated bandwidth, Δf is the subcarrier spacing, T_{tt} is the total transmission time, and T is the symbol duration. In one OTFS frame, the number of grids in the delay domain is $N_\tau = B/\Delta f$ and the number of grinds in the Doppler domain is $N_v = T_{tt}/T$; thus, the total number of grids is $N_\tau \times N_v$. Let $w(k, l)$, $k = 0, ..., N_v - 1$, $l = 0, ..., N_\tau - 1$ be the constellation points of an M-ary QAM treated as points in the DD domain. Then, the output of ISFFT is given by

$$W(m, n) = \frac{1}{\sqrt{N_\tau N_v}} \sum_{k=0}^{N_v-1} \sum_{l=0}^{N_\tau-1} w(k,l)\, e^{-j2\pi\left(\frac{nl}{N_\tau} - \frac{km}{N_v}\right)}, \quad m = 0, 1, ..., N_v - 1;\ n = 0, 1, ..., N_\tau - 1. \tag{1}$$

The output of the SI block is given by

$$X(i, n) = \frac{1}{\sqrt{N_v}} \sum_{m=0}^{N_v-1} W(m, n)\, e^{j2\pi\frac{mi}{N_v}}, \quad i = 0, 1, ..., N_v - 1;\ n = 0, 1, ..., N_\tau - 1. \tag{2}$$

The output of the Heisenberg transform is given by

$$x(t) = \frac{1}{\sqrt{N_\tau}} \sum_{i=0}^{N_v-1} \sum_{n=0}^{N_\tau-1} X(i, n) g_w(t - iT) e^{j2\pi n\Delta f(t-iT)}, \tag{3}$$

where g_w is a transmit rectangular windowing function consisting of all ones. The μ-law and A-law operations on the time-domain signal, $x(t)$, can be expressed as follows [14]:

$$y_\mu(t) = B\frac{\log(1+\mu|x(t)|)}{\log(1+\mu)}\text{sign}(x(t)), \tag{4}$$

and

$$y_A(t) = \begin{cases} \dfrac{CA|x(t)|}{1+\log A}\text{sign}(x(t)), & 0 < |x(t)| \le \dfrac{\gamma}{A}, \\ \dfrac{C\gamma + C\gamma\log\left(\dfrac{A|x(t)|}{\gamma}\right)}{1+\log A}\text{sign}(x(t)), & \dfrac{\gamma}{A} < |x(t)| \le \gamma, \end{cases} \tag{5}$$

where μ and A are the companding parameters of the μ-law and A-laws, respectively. $|\cdot|$ denotes the absolute value, sign$(\cdot)$ denotes signum function, and $\gamma = \max_t |x(t)|$. Constants B and C ensure that the average powers of $y_\mu(t)$ and $y_A(t)$ are the same as those of $x(t)$. Constants B and C are given by

$$B = \log(1+\mu)\sqrt{\frac{\mathbb{E}\left[|x(t)|^2\right]}{\mathbb{E}\left[|\log(1+\mu|x(t)|)|^2\right]}}, \tag{6}$$

and

$$C = (1+\log A)\sqrt{\frac{\mathbb{E}\left[|x(t)|^2\right]}{P_{x1}+P_{x2}}}, \tag{7}$$

where $P_{x1} = A^2\,\mathbb{E}\left[|x(t)|^2\right]$ for $0 < |x(t)| \le \gamma/A$, $P_{x2} = \gamma^2\,\mathbb{E}\left[|1+\log(A|x(t)|/\gamma)|^2\right]$ for $\gamma/A < |x(t)| \le \gamma$, and $\mathbb{E}$ is an expectation operator.

After adding the CP, the resulting signal is amplified by a solid-state power amplifier (SSPA). The output is then given by

$$z(t) = \frac{D_g \cdot |y(t)|\angle \text{y(t)}}{\left[1 + \left(\frac{|y(t)|}{D_{sat}}\right)^{2p}\right]^{\frac{1}{2p}}}, \tag{8}$$

where D_g and D_{sat} denote the gain and saturation levels of the SSPA, respectively, p is a positive number for controlling the nonlinearity of SSPA, and $\angle$y(t) denotes an argument of the signal $y(t)$. Note that $y(t)$ means either $y_\mu(t)$ or $y_A(t)$, depending on whether the companding μ-law or A-law is used.

At the receiver, after removing the CP, either the inverse μ-law or inverse A-law is applied. The operation of the inverse μ-law is expressed as

$$\tilde{x}(t) = \frac{1}{\mu}\left[(1+\mu)^{\left(\frac{|r(t)|}{A}\right)} - 1\right]\text{sign}(r(t)), \tag{9}$$

where $r(t)$ is the signal received after removing the CP. The operation of the inverse A-law is given by

$$\tilde{x}(t) = \begin{cases} \dfrac{|r(t)|\alpha}{A}\text{sign}(r(t)), & 0 \le |r(t)| \le \dfrac{\gamma}{\alpha}, \\ \dfrac{\gamma}{A}\exp\left(\dfrac{|r(t)|\alpha}{\gamma} - 1\right)\text{sign}(r(t)), & \dfrac{\gamma}{\alpha} < |r(t)| \le \gamma, \end{cases} \tag{10}$$

where $\alpha = (1+\log A)/C$. The inverse companding transform output is then fed into the Wigner transform. The output of the Wigner transform is in the time–frequency domain, and the sampled version of the output at $t = iT$ and $f = n\Delta f$ is given by

$$\tilde{X}(i, n) = \int \tilde{x}(t) g_w^*(t - iT) e^{-j2\pi n\Delta f(t-iT)} dt, \quad i = 0, 1, ..., N_v - 1;\ n = 0, 1, ..., N_\tau - 1. \tag{11}$$

The operation of the symbol despreading block is expressed as

$$\tilde{W}(m, n) = \frac{1}{\sqrt{N_v}} \sum_{i=0}^{N_v-1} \tilde{X}(i, n)\, e^{-j2\pi \frac{mi}{N_v}}, \quad m = 0, 1, \ldots, N_v - 1;\ n = 0, 1, \ldots, N_\tau - 1. \tag{12}$$

The output of the SFFT operation is given by

$$\tilde{w}(k, l) = \frac{1}{\sqrt{N_\tau N_v}} \sum_{m=0}^{N_v-1} \sum_{n=0}^{N_\tau-1} \tilde{W}(m, n)\, e^{j2\pi\left(\frac{nl}{N_\tau} - \frac{mk}{N_v}\right)}, \quad k = 0, 1, \ldots, N_v - 1;\ l = 0, 1, \ldots, N_\tau - 1. \tag{13}$$

Finally, data points $\tilde{w}(k,l)$ in the DD are mapped back to the original information format to compute the errors.

3 | SIMULATION RESULTS

This section describes the simulation results and performance analyses of the OTFS μ-law [14], SI OTFS [15], proposed SI OTFS μ-law, and SI OTFS A-law systems. The metrics considered in this study for performance analyses are PAPR values, CCDF of PAPR, CCDF of IAPR, PDF, and BER. The results are also presented for different values of the delay (N_τ) and Doppler (N_v) bins in different modulation formats. For the simulation, we considered a CP of length three, which is the maximum number of delay taps, and a complex additive white Gaussian channel with zero mean and variance σ^2. The noise variance, σ^2, was determined from the given average bit energy-to-noise ratio (E_b/N_o) and the average bit energy of a particular modulation format. The smoothness factor of the SSPA was set to $p = 1.2$. All results were averaged over 10^4 randomly executed frames. In the case of the OTFS μ-law or the SI OTFS μ-law, the μ value was taken as 1.45, as it is the optimal value mentioned in [14]. For A-law companding, A value is considered to be $A = 3.26$ [14].

Table 1 compares the PAPR values of the OTFS μ-law [14], SI OTFS [15], proposed SI OTFS μ-law, and SI OTFS A-law systems for different values of the delay (N_τ) and Doppler (N_v) bins. The mapping format used was 16-QAM. For N_v and N_τ, we compared PAPR values of the OTFS system with identical frame sizes (i.e., $N_v \times N_\tau$) using different combinations of N_v and N_τ. For example, the PAPR values of the OTFS system with frame sizes of 2048, 4096, and 8192 were 7.62, 8.21, and 9.18, respectively, when $(N_v, N_\tau) = (16, 128)$, (16, 256), and (32, 256). However, the PAPR values were 7.92, 8.56, and 9.38 when $(N_v, N_\tau) = (32, 64)$, (32, 128), and (64, 128). It is important to note that the frame sizes were identical (i.e., $N_v \times N_\tau = 2048$ for values $(N_v, N_\tau) = (16, 128)$ and $(N_v, N_\tau) = (32, 64)$). However, the PAPR values were 7.62 and 7.92. These results clearly indicate that the PAPR of the OTFS system depends on the number of symbols, N_v. Among the different approaches, SI-based OTFS systems (i.e., SI OTFS, SI OTFS μ-law, and SI OTFS A-law) provided constant PAPRs irrespective of N_v and N_τ, owing to the data spread across all N_v symbols.

Table 2 lists the PAPR values comparison of all methods and different mapping formats, including quadrature phase-shift keying (QPSK), 8-QAM, 16-QAM, 32-QAM, 64-QAM, and 256-QAM. The numbers of symbols and subcarriers were $N_v = 32$ and $N_\tau = 64$, respectively. The results in Table 2 indicate that the PAPR of SI-based approaches is liable to change with the modulation order because data spreading is independent of the QAM order, and the PAPR of the OTFS system increases with modulation order. Note that the SI OTFS system has a low PAPR until the modulation order reaches 32-QAM,

TABLE 1 PAPR of OTFS, OTFS μ-law, SI OTFS, SI OTFS μ-law, and SI OTFS A-law for different values of N_v and N_τ.

N_v, N_τ	OTFS	OTFS μ-law	SI OTFS	Proposed (μ-law, A-law)
16, 32	6.46	2.52	1.79	1.41, 1.46
16, 64	7.05	2.61	1.79	1.41, 1.46
16, 128	7.62	2.67	1.79	1.41, 1.46
16, 256	8.21	2.75	1.79	1.41, 1.46
32, 64	7.92	2.72	1.79	1.41, 1.46
32, 128	8.56	2.79	1.79	1.41, 1.46
32, 256	9.18	2.86	1.79	1.41, 1.46
64, 128	9.38	2.88	1.79	1.41, 1.46
64, 256	10.06	2.96	1.79	1.41, 1.46
128, 256	10.85	3.04	1.79	1.41, 1.46

TABLE 2 PAPR of OTFS, OTFS μ-law, SI OTFS, SI OTFS μ-law, and SI OTFS A-law for different modulation formats.

Mapping	OTFS	OTFS μ-law	SI OTFS	Proposed (μ-law, A-law)
QPSK	7.79	3.36	1	1, 1
8-QAM	8.21	2.94	1.66	1.41, 1.43
16-QAM	7.92	2.72	1.79	1.41, 1.46
32-QAM	7.93	2.51	1.69	1.34, 1.41
64-QAM	7.96	2.32	2.33	1.47, 1.69
256-QAM	7.94	2.04	2.65	1.44, 1.83

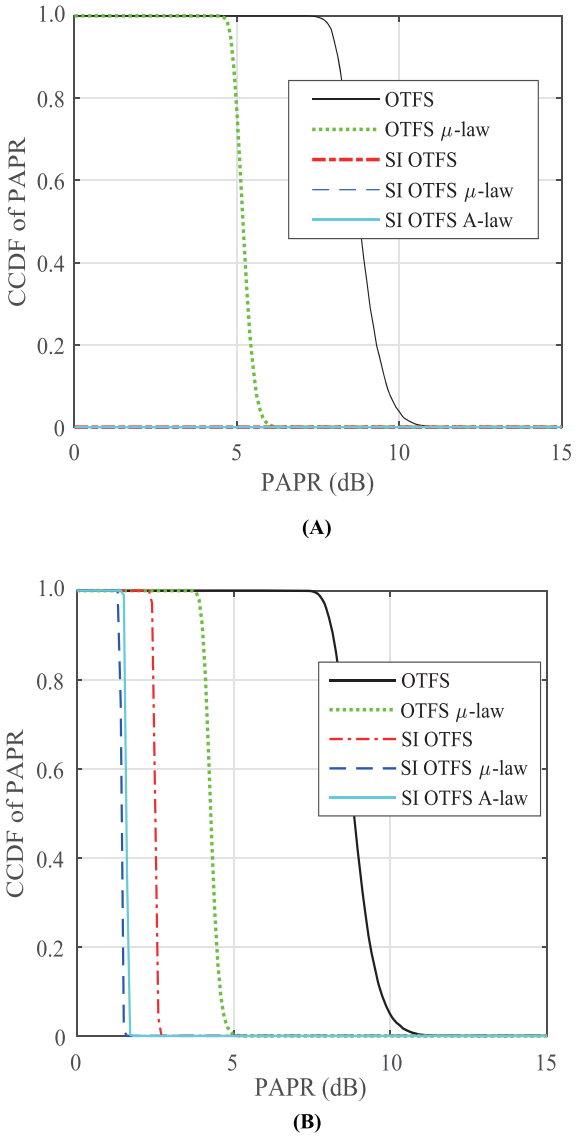

FIGURE 2 CCDF of PAPR in OTFS, OTFS μ-law [14], SI OTFS [15], SI OTFS μ-law, and SI OTFS A-law systems: (A) $N_v = 32, N_\tau = 64,$ and QPSK and (B) $N_v = 32, N_\tau = 64,$ and 16-QAM.

and it has a high PAPR beyond 64-QAM, compared with the OTFS μ-law approach. However, the proposed system, particularly with the SI OTFS μ-law approach, obtained a low PAPR.

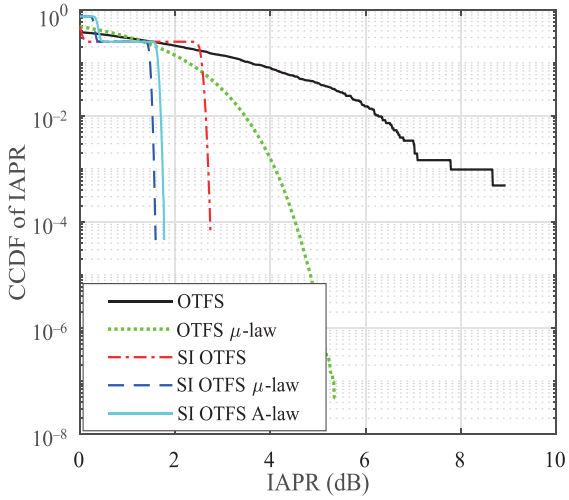

FIGURE 3 CCDF of IAPR in OTFS, OTFS μ-law [14], SI OTFS [15], SI OTFS μ-law, and SI OTFS A-law systems.

Figures 2 and 3 illustrate the CCDF of PAPR and CCDF of IAPR, respectively, for all methods for performance comparison. We set $N_v = 32$ and $N_\tau = 64$. The mapping format was QPSK in Figure 2A and 16-QAM in Figures 2B and 3. In Figure 2A, the CCDF curves of the SI OTFS, SI OTFS μ-law, and SI OTFS A-law approached the horizontal axis when the CCDF of PAPR was zero. This indicates that the PAPRs of these three approaches were always less than a given PAPR threshold; thus, the probability was one and the CCDF was zero. Overall, the PAPR results in Tables 1 and 2 and the CCDF results in Figures 2 and 3 indicate that the proposed SI OTFS μ-law and SI OTFS A-law systems achieved a low PAPR/IAPR for any number of symbols, any number of subcarriers, and any order of modulation compared with OTFS, OTFS μ-law [14], and SI OTFS [15] systems.

The PDFs of the PAPR values of (A) OTFS, (B) OTFS μ-law [14], (C) SI OTFS [15], (D) SI OTFS μ-law, and (E) SI OTFS A-law systems are given for different values of Doppler bins $N_v = \{32, 64, 128\}$ in Figure 4 and for different QAM formats {16-QAM, 64-QAM, 256-QAM} in Figure 5. We set the other parameters to $N_\tau = 256$ and 64-QAM/$N_v = 128$. Based on the PDFs, we observed that

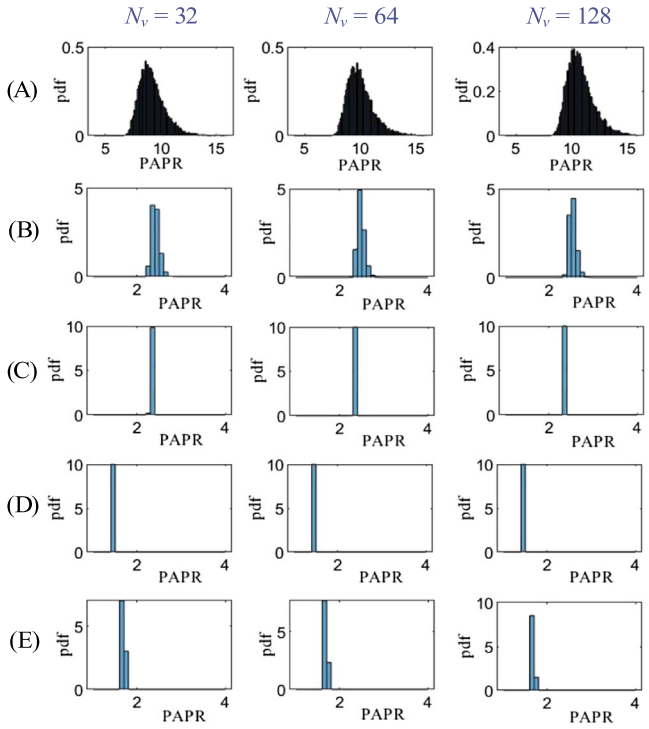

FIGURE 4 Probability density functions of (A) OTFS, (B) OTFS μ-law [14], (C) SI OTFS [15], (D) SI OTFS μ-law, and (E) SI OTFS A-law systems for $N_v = 32$, $N_v = 64$, and $N_v = 128$.

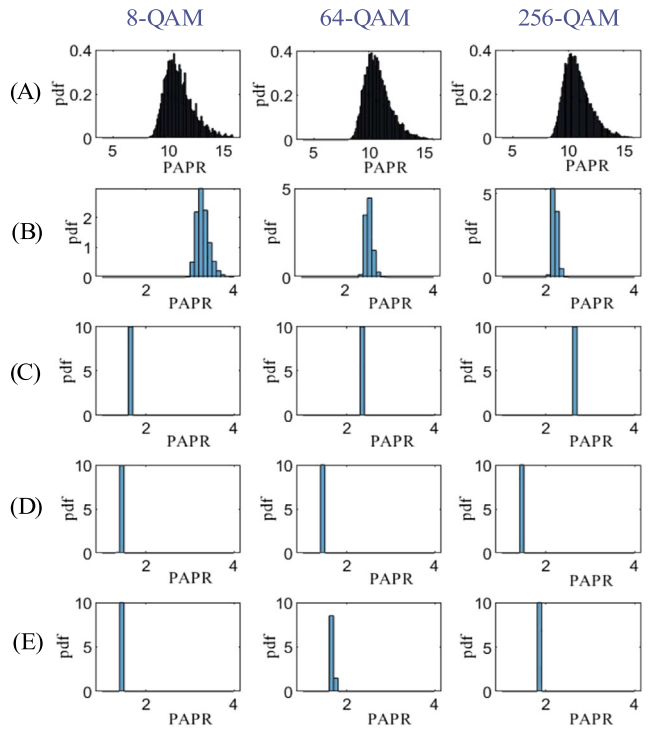

FIGURE 5 Probability density functions of (A) OTFS, (B) OTFS μ-law [14], (C) SI OTFS [15], (D) SI OTFS μ-law, and (E) SI OTFS A-law systems for 16-QAM, 64-QAM, and 256-QAM.

the PAPR values of the OTFS and OTFS μ-law [14] systems followed a Rayleigh distribution, whereas the distribution was uniform in the SI OTFS [15] and SI OTFS μ-law systems; it was nearly uniform in the SI OTFS A-law system. In the OTFS, the lower bound of the Rayleigh distribution was different for different Doppler bins; however, it was constant for different QAM formats. In the OTFS μ-law, the scale parameter of the Rayleigh distribution was different for different Doppler bins and QAM formats. The lower bound was different for different QAM formats but was constant for different Doppler bins. The scale parameter of the uniform distribution was constant in both SI OTFS and SI OTFS μ-law systems. For SI OTFS and SI OTFS A-law, the location parameter

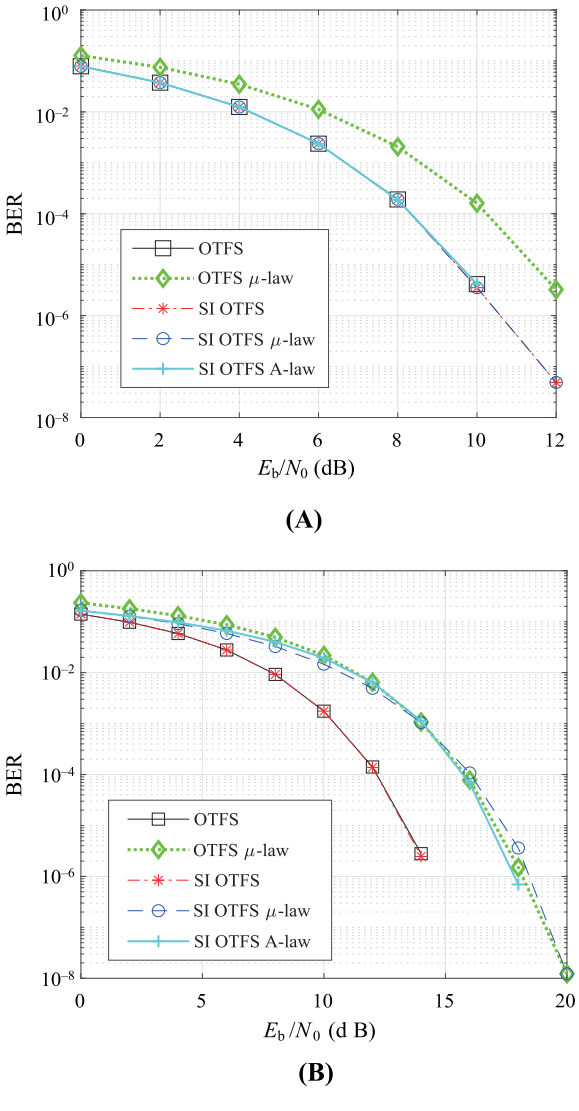

FIGURE 6 BER performance of the OTFS, OTFS μ-law [14], SI OTFS [15], SI OTFS μ-law, and SI OTFS A-law systems without HPA: (A) $N_v = 32, N_\tau = 64$, and QPSK and (B) $N_v = 32, N_\tau = 64$, and 16-QAM.

of the uniform distribution differed for different QAM formats, whereas for SI OTFS μ-law, the location parameter was constant. The PDF of the SI OTFS μ-law was uniform and was located in the low PAPR region.

Figures 6–8 show the BER performances of the OTFS, OTFS μ-law [14], SI OTFS [15], and the proposed SI OTFS μ-law and SI OTFS A-law systems in the absence of HPA, respectively, as well as the presence of HPA. In this analysis, we set $N_v = 32$ and $N_\tau = 64$. The mapping format was QPSK in Figures 6A, 7A, and 8A, 16-QAM in Figures 6B and 7B, and 64-QAM in Figure 8B. Furthermore, Figure 6 evaluates the BER performance without HPA (SSPA) at the transmitter, and Figures 7 and 8 examine the SSPA with an input backoff (IBO) of 10 and 5 dB, respectively. The BER curves in Figures 6 and 7 indicate that the OTFS system with SSPA required an IBO of 10 dB to obtain a performance equivalent to that of the system without HPA, and the BER performance of the SI OTFS system was the same as that of the OTFS system. As the modulation order increased from QPSK to 16-QAM, the proposed SI OTFS μ-law system exhibited poor BER performance relative to the OTFS and SI OTFS systems. The poor BER performance was caused by the amplification of channel noise during inverse companding. From Figure 8, we can observe that the BER performances of the SI OTFS and SI OTFS A-law systems were better than those of the OTFS when the dynamic range of the HPA was insufficient relative to the required dynamic range for the OTFS signal, which was 10 dB.

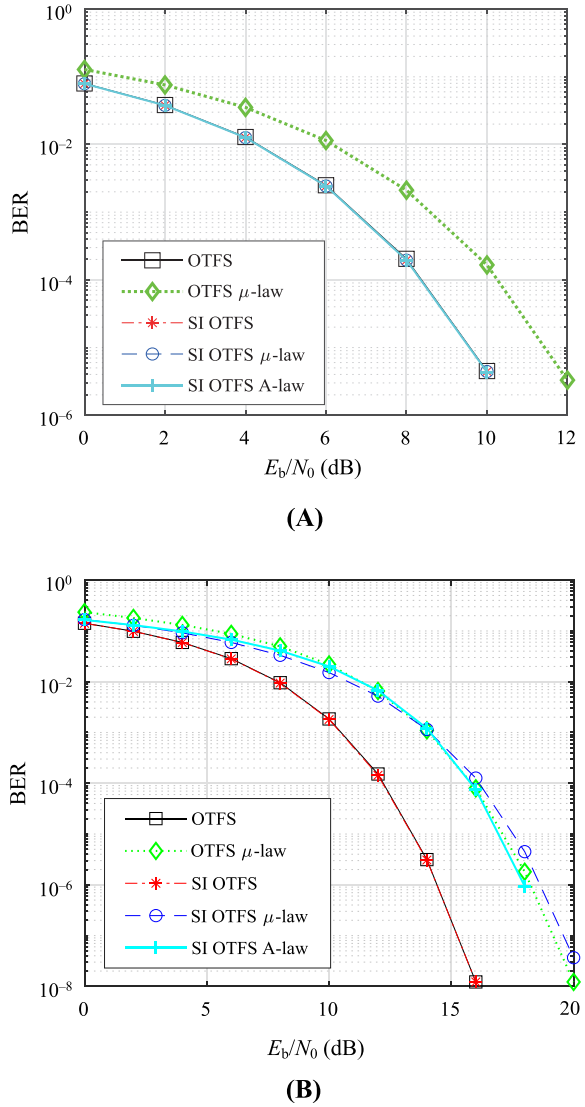

FIGURE 7 BER performance of the OTFS, OTFS μ-law [14], SI OTFS [15], SI OTFS μ-law, and SI OTFS A-law systems with a SSPA of IBO = 10 dB: (A) $N_v = 32, N_\tau = 64$, and QPSK and (B) $N_v = 32, N_\tau = 64$, and 16-QAM.

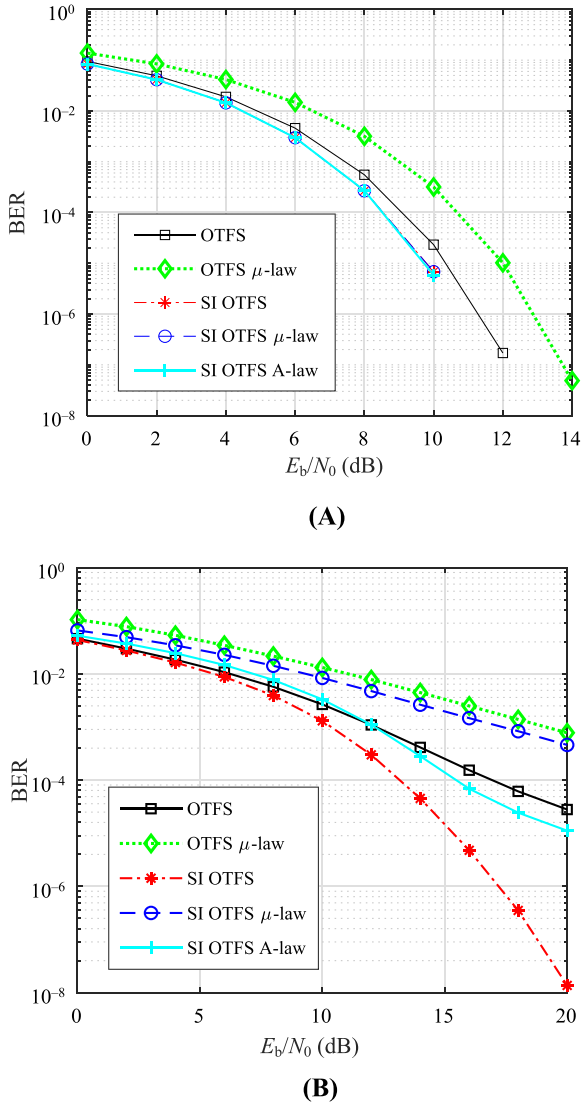

FIGURE 8 BER performance of the OTFS, OTFS μ-law [14], SI OTFS [15], SI OTFS μ-law, and SI OTFS A-law systems with a SSPA of IBO = 5 dB: (A) $N_v = 32, N_\tau = 64$, and QPSK and (B) $N_v = 32, N_\tau = 64$, and 64-QAM.

Overall, among all methods analyzed in this paper, the proposed SI OTFS A-law system achieved superior performance in terms of both PAPR reduction and BER performance.

4 | CONCLUSION

This study proposed two methods based on SI and μ-law or A-law companding transforms to reduce the PAPR of an OTFS signal. The performance was tested using a solid-state power amplifier at the transmitter. Performance metrics (i.e., CCDF, PDF, and BER) were compared with those of existing methods, revealing that SI combined with A-law companding transform outperforms both the PAPR reduction and BER performance.

CONFLICT OF INTEREST STATEMENT

The authors declare that there are no conflicts of interest.

ORCID

Aare Gopal https://orcid.org/0009-0004-5841-9960

REFERENCES

1. R. Hadani, S. Rakib, M. Tsatsanis, A. Monk, A. J. Goldsmith, A. F. Molisch, and R. Calderbank, *Orthogonal time-frequency space modulation*, (IEEE Wireless Commun. Networking Conf., IEEE, San Francisco, CA, USA), 2017, pp. 1–6.
2. G. Surabhi, R. M. Augustine, and A. Chockalingam, *Peak-to-average power ratio of OTFS modulation*, IEEE Commun. Lett. **23** (2019), no. 6, 999–1002.
3. N. A. Sivadas, *PAPR reduction of OFDM systems using the H-SLM method with a multiplierless IFFT FFT technique*, ETRI J. **44** (2022), 379–388.
4. K. Anwar and H. Yamamoto, *A new design of carrier interferometry OFDM with FFT as spreading codes*, (Proc. IEEE Radio Wireless Sympos., IEEE, San Diego, CA, USA), 2006, pp. 543–546.
5. X. Wang, T. T. Tjhung, C. Sum Ng, and A. Ali Kassim, *On the SER analysis of A-law companded OFDM system*, (IEEE Global Telecommun. Conf., IEEE, San Francisco, CA, USA), 2000, pp. 756–760.
6. Y. A. Al-Jawhar, K. N. Ramli, M. A. Taher, N. S. M. Shah, S. A. Mostafa, and B. A. Khalaf, *Improving PAPR performance of filtered OFDM for 5G communications using PTS*, ETRI J. **43** (2021), 209–220.
7. M. N. Hossain, Y. Sugiura, T. Shimamura, and H. G. Ryu, *DFT-Spread OTFS communication system with the reductions of PAPR and nonlinear degradation*, Wirel. Personal Commun. **115** (2020), no. 3, 2211–2228.
8. S. Gao and J. Zheng, *Peak-to-average power ratio reduction in pilot-embedded OTFS modulation through iterative clipping and filtering*, IEEE Commun. Lett. **24** (2020), no. 9, 2055–2059.
9. M. Liu, M. M. Zhao, M. Lei, and M. J. Zhao, *Autoencoder based PAPR reduction for OTFS modulation*, (IEEE 94th Veh. Technol. Conf., IEEE, Norman, OK, USA), 2021, pp. 1–5.
10. A. S. Sümer, T. Yılmaz, E. Memişoğlu, and H. Arslan, *Exploiting OTFS frame structure for PAPR reduction*, (IEEE 96th Veh. Technol. Conf., IEEE, London, UK), 2022, pp. 1–5.
11. H. Shang, R. Chen, H. Zhang, G. Ma, R. He, B. Ai, and Z. Zhong, *OTFS modulation and PAPR reduction for IoT-railways*, China Commun. **20** (2023), no. 1, 102–113.
12. C. Naveen and V. Sudha, *Peak-to-average power ratio reduction in OTFS modulation using companding technique*, (5th IEEE Int. Conf. Devices Circuits Syst., IEEE, Coimbatore, India), 2020, pp. 140–143.
13. B. Hanumantharao, P. Palanisamy, C. Srinivasarao, and P. Salai, *Exponential companding technique for PAPR reduction in OTFS signals*, Phys. Commun. **53** (2022), 10729.
14. B. Hanumantharao, P. Palanisamy, and C. Srinivasarao, *Reduction of PAPR in OTFS using normalized μ-law and A-law companding transform*, Int. Technol. Lett. **5** (2022), no. 3, 1–6.
15. A. Gopal, D. K. Reddy, and S. Chintagunta, *Symbol interferometry for PAPR reduction of OTFS modulation*, (IEEE Second Int. Conf. Next Gener. Intell. Syst., IEEE, Kottayam, India), 2022, pp. 1–4.

AUTHOR BIOGRAPHIES

Aare Gopal received his B.Tech. and M.Tech. degrees in Electronics and Communication Engineering from the Jawaharlal Nehru Technological University, Hyderabad, India, in 2003 and 2011, respectively. He is currently pursuing a Ph.D. in electronics and communication engineering from Osmania University in Hyderabad. His primary research interests include wireless communication and signal processing.

Desireddy Krishna Reddy obtained his B.E. degree with distinction from Andhra University, Waltair, India, and his M.E. degree with specialization in Microwaves and Radar Engineering from Osmania University, Hyderabad, India. He received his Ph.D. from Osmania University in 2008. He has 30 years of experience in teaching, research, and development. He is currently a professor and the head of the Department of Electronics and Communication Engineering at CBIT in Hyderabad. His research interests include GNSS, 5G, and mobile communications.

Srinivasarao Chintagunta received his M.Tech. degree in signal processing from the National Institute of Technology, Calicut, India, in 2010, and his Ph.D. degree from the National Institute of Technology, Tiruchirappalli, India, in 2018. He is currently an assistant professor in the Department of Electronics and Communication Engineering, National Institute of Technology, Calicut, India. His research interests include array signal processing, MIMO radars, and wireless communication.

How to cite this article: A. Gopal, D. K. Reddy, and S. Chintagunta, *Symbol interferometry and companding transform for PAPR reduction of OTFS signal*, ETRI Journal **46** (2024), 595–603. DOI 10.4218/etrij.2023-0142